

Tracking an eruptive prominence using multiwavelength and multiview observations on 2023 March 7

QINGMIN ZHANG,^{1,2} YUDI OU,^{1,3} ZHENGHUA HUANG,⁴ YONGLIANG SONG,⁵ AND SULI MA²

¹Key Laboratory of Dark Matter and Space Astronomy, Purple Mountain Observatory, CAS, Nanjing 210023, People's Republic of China

²State Key Laboratory of Space Weather, National Space Science Center, Chinese Academy of Sciences, Beijing 100190, People's Republic of China

³Department of Astronomy and Space Science, University of Science and Technology of China, Hefei 230026, People's Republic of China

⁴Shandong Key Laboratory of Optical Astronomy and Solar-Terrestrial Environment, Institute of Space Sciences, Weihai 264209, People's Republic of China

⁵National Astronomical Observatories, Chinese Academy of Sciences, Beijing 100101, People's Republic of China

ABSTRACT

In this paper, we carry out multiwavelength and multiview observations of the prominence eruption, which generates a C2.3 class flare and a coronal mass ejection (CME) on 2023 March 7. For the first time, we apply the revised cone model to three-dimension reconstruction and tracking of the eruptive prominence for ~ 4 hrs. The prominence propagates non-radially and makes a detour around the large-scale coronal loops in active region NOAA 13243. The northward deflection angle increases from $\sim 36^\circ$ to $\sim 47^\circ$ before returning to $\sim 36^\circ$ and keeping up. There is no longitudinal deflection throughout the propagation. The angular width of the cone increases from $\sim 30^\circ$ and reaches a plateau at $\sim 37^\circ$. The heliocentric distance of the prominence rises from ~ 1.1 to $\sim 10.0 R_\odot$, and the prominence experiences continuous acceleration ($\sim 51 \text{ m s}^{-2}$) over two hours, which is probably related to the magnetic reconnection during the C-class flare. The true speed of CME front is estimated to be $\sim 829 \text{ km s}^{-1}$, which is ~ 1.2 times larger than that of CME core (prominence). It is concluded that both acceleration and deflection of eruptive prominences in their early lives could be reproduced with the revised cone model.

Keywords: Sun: prominences — Sun: flares — Sun: coronal mass ejections (CMEs)

1. INTRODUCTION

Prominences are prevalent in the solar atmosphere (Vial & Engvold 2015). The density and temperature are nearly two orders of magnitude higher and lower than the corona (Labrosse et al. 2010; Mackay et al. 2010; Parenti 2014). On the solar disk, prominences appear as dark filaments due to the absorption of emission from the chromosphere. High-resolution observations in H α and Ca II 396.8 nm H line reveal that prominences (or filaments) are composed of a bundle of ultrafine and dynamic threads (e.g., Zirker et al. 1998; Lin et al. 2005; Okamoto et al. 2007; Berger et al. 2010; Yan et al. 2015; Yang et al. 2017; Wei et al. 2023; Wang et al. 2024; Zhang et al. 2024a). The magnetic configurations holding prominences are sheared arcades (Karpen et al. 2005), magnetic flux ropes (MFRs; Rust & Kumar 1996; Ruan et al. 2014; Xia & Keppens 2016; Zhang et al. 2022), or both (Guo et al. 2010; Liu et al. 2012; Awasthi et al. 2019; Hou et al. 2023). After losing a stabil-

ity, the successful eruption of a prominence may lead to a solar flare (Fletcher 2024) and a coronal mass ejection (CME; Chen 2011; Georgoulis et al. 2019; Kilpua et al. 2019).

Owing to the projection effect, the three-dimensional (3D) morphology and evolution of a filament is unknown from a single view. The magnetic topology of a filament before eruption is obtainable using the nonlinear force-free field (NLFFF) modelings, such as the optimization method (Wiegmann et al. 2006; Hou et al. 2023), stress-and-relax method (Valori et al. 2005), and flux rope insertion method (van Ballegooijen 2004; Teng et al. 2024). The early evolutions of filaments up to $2\text{--}3 R_\odot$ could be derived with the help of sophisticated data-constrained magnetohydrodynamics (MHD) simulations (Zhong et al. 2021; Guo et al. 2023). Successive launches of twin spacecrafts of the Solar TERrestrial RELations Observatory (STEREO; Kaiser et al. 2008) and the Solar Dynamics Observatory (SDO; Pesnell et al. 2012) spacecraft enable 3D reconstructions of prominences simultaneously observed from two or three viewing angles using the tie-pointing or triangulation method (Bemporad 2009; Liewer et al. 2009; Joshi & Srivastava 2011; Li et al. 2011; Panasenco et al.

2011; Thompson 2011; Thompson et al. 2012; Shen et al. 2012; Howard 2015; Zhou et al. 2017; Guo et al. 2019; Zhou et al. 2021; Sahade et al. 2023; Zhang et al. 2024b).

For the 3D reconstruction of CMEs, a large number of techniques have been proposed (e.g., Moran & Davila 2004; Howard et al. 2006; Mierla et al. 2008, 2010; Feng et al. 2012). In the forward modeling type, a couple of geometrical models have been developed, such as the cone model (Zhao et al. 2002; Michałek et al. 2003; Xie et al. 2004), Graduated Cylindrical Shell (GCS; Thernisien et al. 2006) model, FRiED model (Isavnin 2016), and 3DCORE model (Weiss et al. 2021). Considering that plenty of CMEs are generated by non-radial prominence eruptions (Bi et al. 2013; Zhang et al. 2022; Sahade et al. 2023), Zhang (2021) slightly revised the traditional cone model by introducing two angles: one is inclination angle (θ_1) from the local vertical, the other is inclination angle (ϕ_1) from the local meridian plane. The shape and total length of the cone leading edge are adjustable depending on the events of interest (Schwenn et al. 2005; Zhang 2022). Dai et al. (2023) investigated the large-amplitude, transverse oscillation of a quiescent filament on 2022 October 2. The oscillation is excited by a propagating extreme-ultraviolet (EUV) wave in the north-east direction, which is generated by the non-radial filament eruption from active region (AR) NOAA 13110. The 3D shape of the erupting loops in front of the erupting filament is derived using the revised cone model. Recently, Zhang et al. (2023a) made a slight modification to the GCS model and applied it to the 3D reconstruction of an eruptive prominences originating from AR 13110 on 2022 September 23. Acceleration and southward deflection of the prominence during its early evolution are nicely reproduced.

On 2023 March 7, a prominence erupted to the north of AR 13243 (N18W90) close to the western limb, generating a C2.3 class flare and a wide CME. Fortunately, the prominence was observed by a fleet of instruments from multiple viewpoints, including the Global Oscillation Network Group (GONG), the Atmospheric Imaging Assembly (AIA; Lemen et al. 2012) on board SDO, the Extreme-Ultraviolet Imager (EUVI; Howard et al. 2008) and COR2 coronagraph on board the ahead STEREO (hereafter STA), the Solar Ultraviolet Imager (SUVI; Seaton & Darnel 2018; Tadikonda et al. 2019) on board the GOES-16 spacecraft, the Full Sun Imager (FSI) of the Extreme Ultraviolet Imager (EUI; Rochus et al. 2020) on board Solar Orbiter (SoIo; Müller et al. 2020), and the C2 and C3 coronagraphs of the Large Angle Spectroscopic Coronagraph (LASCO; Brueckner et al. 1995) on board the Solar and Heliospheric Observatory (SOHO) mission. Soft X-ray (SXR) fluxes of the C2.3 flare in 1–8 Å were recorded by the GOES-16 spacecraft. In Figure 1, the Solar-MACH plot (Gieseler et al. 2023) shows the locations of STA (red box), SoIo (blue

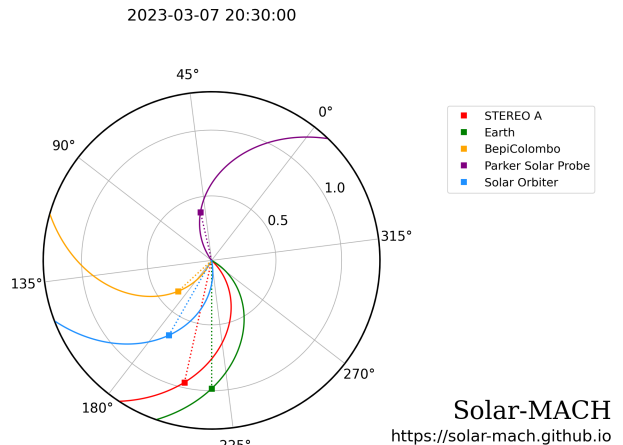


Figure 1. The Solar-MACH plot at 20:30 UT on 2023 March 7, showing the locations and connectivity to the Sun of STA (red box), SoIo (blue box), and Earth (green box).

box), and Earth (green box), respectively. The properties of these instruments are summarized in Table 1, including the wavelengths, pixel sizes, time cadences, heliocentric distances, longitudinal (ϕ_0) and latitudinal (θ_0) separation angles with the Sun-Earth line. The prominence is believed to be the bright core of the typical three-part structure of a CME observed in white-light (WL) coronagraphs (Illing & Hundhausen 1985; Howard 2015; Song et al. 2023; Zhou et al. 2023). Zhang (2021) applied the revised cone model to the leading edges of two CMEs observed in EUV wavelengths. In the current study, we apply the same model to the prominence itself. Multiwavelength and multiview observations enable us to carry out 3D reconstruction and tracking of the eruptive prominence up to $\sim 10 R_{\odot}$. The paper is organized as follows. We describe method and data analysis in Section 2. The results are presented in Section 3. Discussions and a brief conclusion are given in Section 4 and Section 5, respectively.

2. METHOD AND DATA ANALYSIS

The level_1 data of AIA are calibrated using the `aia_prep.pro` in *Solar Software* (SSW). The GONG $H\alpha$ images are coaligned with the AIA 304 Å images using the cross correlation method. The STA/EUVI images are calibrated using the `secchi_prep.pro` and rotated by a certain angle to align with the solar north. The level_2 data of EUI/FSI are processed using the `eui_readfits.pro` and rotated to align with the solar north as well. The SUVI images are also rotated and shifted slightly to align with the AIA images. Base-difference images of these instruments are obtained to highlight the eruptive prominence, especially when the prominence propagates far away from the solar surface and its emission decreases sharply.

Table 1. Wavelengths, pixel sizes, cadences, heliocentric distances, longitudinal and latitudinal separation angles with the Sun-Earth line of the instruments on 2023 March 7.

Instrument	λ (Å)	Pix. size (")	Cadence (second)	Dist. (AU)	ϕ_0 (°)	θ_0 (°)
GONG	6562.8	1.0	60	1.0	0	0
SDO/AIA	94–1600	0.6	12, 24	1.0	0	0
GOES-16/SUVI	304	2.5	100	1.0	0	0
GOES-16	1–8	–	1	1.0	0	0
Solo/EUI	304	4.4	450	0.67	-29.8	3.2
STA/EUVI	304	1.6	600	0.97	-12.6	0
STA/COR2	WL	15.0	900	0.97	-12.6	0
LASCO-C2	WL	11.4	720	0.99	0	0
LASCO-C3	WL	56.0	720	0.99	0	0

In the revised cone model (Zhang 2021, 2022), the source region of an eruptive prominence or a CME is characterized by a longitude (ϕ_2) and a latitude ($\beta_2 = 90^\circ - \theta_2$). The transform between the heliocentric coordinate system (HCS; X_h, Y_h, Z_h) and local coordinate system (LCS; X_l, Y_l, Z_l) is:

$$\begin{pmatrix} x_h \\ y_h \\ z_h \end{pmatrix} = M_2 \begin{pmatrix} x_l \\ y_l \\ z_l \end{pmatrix} + \begin{pmatrix} R_\odot \sin \theta_2 \cos \phi_2 \\ R_\odot \sin \theta_2 \sin \phi_2 \\ R_\odot \cos \theta_2 \end{pmatrix}, \quad (1)$$

where M_2 is a matrix related to θ_2 and ϕ_2 .

The transform between LCS and cone coordinate system (CCS; X_c, Y_c, Z_c) is:

$$\begin{pmatrix} x_l \\ y_l \\ z_l \end{pmatrix} = M_1 \begin{pmatrix} x_c \\ y_c \\ z_c \end{pmatrix}, \quad (2)$$

where M_1 is a matrix related to θ_1 and ϕ_1 . Considering the shape of prominence in this study, the top of the cone is taken to be a sphere (Zhang 2022, see their Fig. 1b). Therefore, the total length of the leading edge is:

$$l = r \left(\tan \frac{\omega}{2} + \left(\cos \frac{\omega}{2} \right)^{-1} \right), \quad (3)$$

where r and ω denote the length of generatrix and angular width of the cone, respectively.

In order to conduct 3D reconstruction of the prominence, multiview observations are required. The transform between HCS and external coordinate system (ECS; X_e, Y_e, Z_e) of STA or Solo is realized by a matrix (M_0):

$$\begin{pmatrix} x_e \\ y_e \\ z_e \end{pmatrix} = M_0 \begin{pmatrix} x_h \\ y_h \\ z_h \end{pmatrix}, \quad (4)$$

where

$$M_0 = \begin{pmatrix} \cos \phi_0 \cos \theta_0 & \sin \phi_0 \cos \theta_0 & -\sin \theta_0 \\ -\sin \phi_0 & \cos \phi_0 & 0 \\ \cos \phi_0 \sin \theta_0 & \sin \phi_0 \sin \theta_0 & \cos \theta_0 \end{pmatrix}, \quad (5)$$

where $\phi_0 = -12.6^\circ$, $\theta_0 = 0^\circ$ for STA and $\phi_0 = -29.8^\circ$, $\theta_0 = 3.2^\circ$ for Solo (see Table 1). The coordinates $[x_e, y_e, z_e]$ are scaled by a factor of heliocentric distances (in unit of AU) using the standard *SSW* routine `scale_map.pro` before transformations. The WL images from LASCO are scaled as well though SOHO is located at L1 point along the Sun-Earth line.

3. RESULTS

3.1. Flare and CME

In Figure 2, panels (a), (b), and (d) show the prominence observed in $H\alpha$, 304 Å, and 171 Å at the beginning of eruption (see also the online animation). The prominence is bright in $H\alpha$ but appears dark in 171 Å due to the low temperature. The inverse- γ shape of the prominence is indicative of a twisted magnetic structure (Ji et al. 2003; Liu et al. 2007). After 20:15 UT, the prominence lifts off slowly, which is probably due to the ideal kink instability (Török et al. 2004; Fan 2005). A bundle of fan-shaped coronal loops rooted in AR 13243 are adjacent to the prominence, which prevent a radial eruption as indicated by the hollow arrow in panel (d) (Panasenco et al. 2013). During the ascent, the prominence expands dramatically, with the two legs standing out not only in 304 Å (panel (c)), but also in 1600 Å (panel (f)). The hot post-flare loops (PFLs) and a pair of conjugate ribbons of the C2.3 flare are obviously demonstrated in 94 Å (panel (e)) and 1600 Å, respectively. To investigate the evolution of the coronal loops, a curved slice (S1) with a length of 312" is selected and drawn with a cyan line in Figure 2(d). Time-distance diagram of S1 in 171 Å is displayed in Figure 3. It is clear that as the prominence rises, the coronal loops are squeezed and quickly pushed aside in the southwest direction during 20:15–20:25 UT. Afterwards, the loops return back gradually and the prominence continues to ascend. In other words, the erupting prominence bypasses the large-scale coronal loops.

In Figure 4, the pink line shows the SXR (1–8 Å) light curve of the flare, which starts at ~20:10 UT and peaks at ~20:46 UT followed by a gradual decay. The dark blue line shows the EUV (94 Å) light curve of the flare with the same trend as in SXR but a delayed peak at ~21:05 UT.

In Figure 5, the top panels show the running-difference images of the CME observed by LASCO-C2 and LASCO-C3 (see also the online animation). The CME first appears at 20:36 UT and propagates in the northwest direction with a central position angle of ~308° and an angular width of

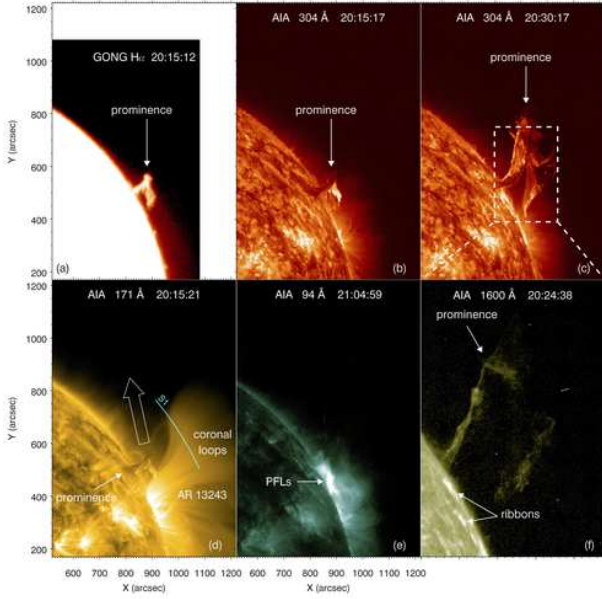


Figure 2. The eruptive prominence and associated flare observed in $H\alpha$ (a), AIA 304 Å (b-c), 171 Å (d), 94 Å (e) and 1600 Å (f) passbands. The solid arrows point to the prominence, post-flare loops (PFLs), and flare ribbons. In panel (c), the white dashed box signifies the field of view (FOV) of panel (f). In panel (d), the hollow arrow indicates the initial direction of eruption. The curved slice S1 is used to investigate the evolution of coronal loops. An animation showing the prominence eruption in 304, 171, and 94 Å is available. It covers a duration of 60 minutes from 20:10 UT to 21:10 UT on 2023 March 7. The entire animation runs for 6 s. (An animation of this figure is available.)

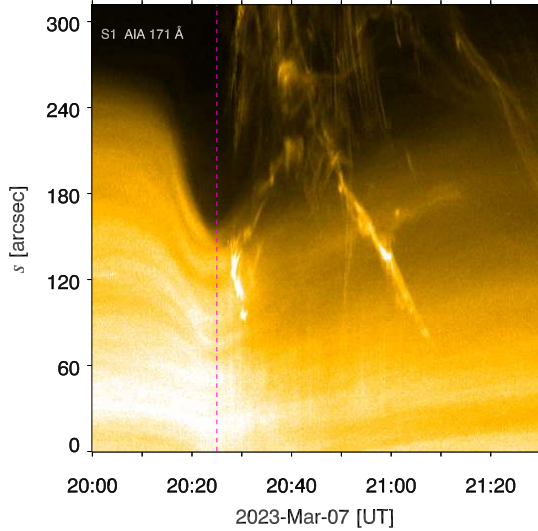


Figure 3. Time-distance diagram of S1 in 171 Å. $s = 0$ and $s = 312''$ stand for the southwest and northeast endpoints of S1 in Figure 2(d), respectively. The magenta dashed line denotes the time (20:25:09 UT) when the coronal loops are pushed farthest by the eruptive prominence.

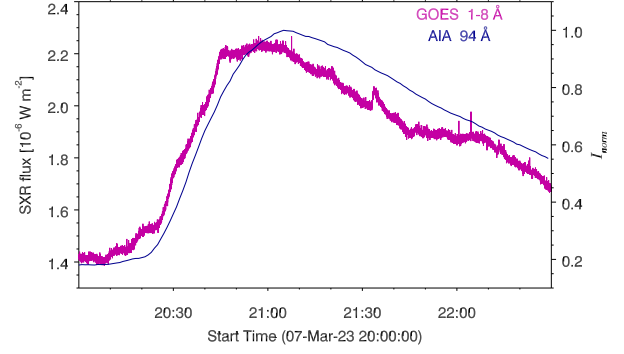


Figure 4. Light curves of the C2.3 flare in 1–8 Å (pink line) and 94 Å (dark blue line).

$\sim 160^\circ$ (partial halo CME¹). In panels (a3)-(a4), the thin arrows point to the eruptive prominence, which evolves into the bright core of CME (Illing & Hundhausen 1985). The bottom panels of Figure 5 show the running-difference images of the CME observed by STA/COR2 during 21:23–23:38 UT.

3.2. 3D reconstruction and tracking of the prominence

To perform 3D reconstruction of the prominence, we expect simultaneous observations from different viewpoints. However, as indicated in Table 1, time cadences of the instruments are inconsistent. Hence, we will first utilize images observed practically simultaneous. In Figure 6, the top panels show the prominence observed in 304 Å by SDO/AIA (a1), GOES-16/SUVI (b1), SoI/O/EUI (c1), and STA/EUVI (d1) around 20:45 UT. In general, the prominence has a similar shape, although the details are distinctive owing to the different viewing angles, dynamic ranges, and FOVs. The prominence is most complete in EUI image with a round leading edge (Liu et al. 2007; Mierla et al. 2022; Zhang et al. 2022), while the two legs are close together. On the contrary, both legs are identifiable with considerable separation in AIA and SUVI images. Using three images in panels (b1), (c1), and (d1), the 3D reconstruction at 20:45 UT is performed. The bottom panels of Figure 6 show the same EUV images superposed by projections of reconstructed cone (cyan dots). The corresponding parameters are $\phi_2 = 72^\circ$, $\theta_2 = 63^\circ$, $\beta_2 = 27^\circ$, $\phi_1 = 0^\circ$, $\theta_1 = -40^\circ$, $r = 640'' \approx 461$ Mm, and $\omega = 37^\circ$. The negative value of θ_1 indicates northward deflection of the prominence, while positive values of θ_1 indicate southward deflection (Zhang 2021). $\phi_1 = 0^\circ$ suggests that there is no longitudinal deflection. It is clear that the reconstructed cone conforms with the prominence leading edge ideally, and meanwhile the tip of the cone is located between the two legs.

¹ https://cdaw.gsfc.nasa.gov/CME_list/UNIVERSAL_ver2/2023_03/univ2023_03.html

Table 2. Parameters of the reconstructed cones with the revised cone model (Zhang 2021).

Time (UT)	Single/Multiple	Instruments	ω ($^{\circ}$)	r ($''$)	l ($''$)	h ($''$)	θ_1 ($^{\circ}$)	ϕ_1 ($^{\circ}$)
20:15:12	Single	GONG	30	118	154	1099	-36	0
20:15:41	Multiple	AIA, STA	30	120	156	1102	-36	0
20:16:12	Single	GONG	30	124	162	1106	-36	0
20:17:12	Single	GONG	30	130	169	1113	-36	0
20:18:12	Single	GONG	30	138	180	1122	-36	0
20:19:12	Single	GONG	30	148	193	1134	-36	0
20:20:12	Single	GONG	30	160	209	1148	-36	0
20:25:41	Multiple (Fig. 7)	AIA, STA	34	215	291	1213	-40	0
20:27:18	Single	SUVI	34	250	338	1242	-45	0
20:28:58	Single (Fig. 9)	SUVI	37	280	389	1281	-47	0
20:30:17	Multiple (Fig. 8)	AIA, EUI	37	310	431	1317	-47	0
20:31:18	Single	SUVI	37	320	445	1329	-47	0
20:32:58	Single (Fig. 9)	SUVI	37	340	472	1353	-47	0
20:35:41	Multiple (Fig. 7)	AIA, STA	37	395	549	1419	-47	0
20:36:58	Single	SUVI	37	420	583	1450	-47	0
20:37:53	Multiple (Fig. 8)	AIA, EUI	37	450	625	1486	-47	0
20:39:18	Single (Fig. 9)	SUVI	37	470	653	1524	-44	0
20:40:58	Single	SUVI	37	510	708	1583	-42	0
20:43:18	Single (Fig. 9)	SUVI	37	560	778	1656	-40	0
20:45:17	Multiple (Fig. 6)	STA, SUVI, EUI	37	640	889	1760	-40	0
20:47:18	Single	SUVI	37	650	903	1773	-40	0
20:48:58	Single	SUVI	37	680	945	1812	-40	0
20:51:18	Single	SUVI	37	730	1014	1882	-39	0
20:52:58	Multiple	SUVI, EUI	37	825	1146	2018	-37	0
21:00:20	Single (Fig. 10)	EUI	37	1000	1389	2257	-36	0
21:07:50	Single	EUI	37	1200	1667	2526	-36	0
21:15:20	Single (Fig. 10)	EUI	37	1400	1945	2797	-36	0
21:22:50	Single	EUI	37	1600	2223	3069	-36	0
21:30:20	Single (Fig. 10)	EUI	37	1800	2500	3342	-36	0
21:37:50	Single	EUI	37	2000	2778	3615	-36	0
21:45:20	Single (Fig. 10)	EUI	37	2200	3056	3889	-36	0
22:18:05	Single (Fig. 11)	LASCO-C3	37	3300	4584	5403	-36	0
22:30:05	Single	LASCO-C3	37	3800	5279	6094	-36	0
23:06:05	Single (Fig. 11)	LASCO-C3	37	4400	6112	6923	-36	0
23:18:05	Single	LASCO-C3	37	5100	7084	7892	-36	0
23:30:05	Single (Fig. 11)	LASCO-C3	37	5600	7779	8585	-36	0
23:42:05	Single	LASCO-C3	37	6000	8335	9139	-36	0
23:54:05	Single (Fig. 11)	LASCO-C3	37	6400	8890	9693	-36	0

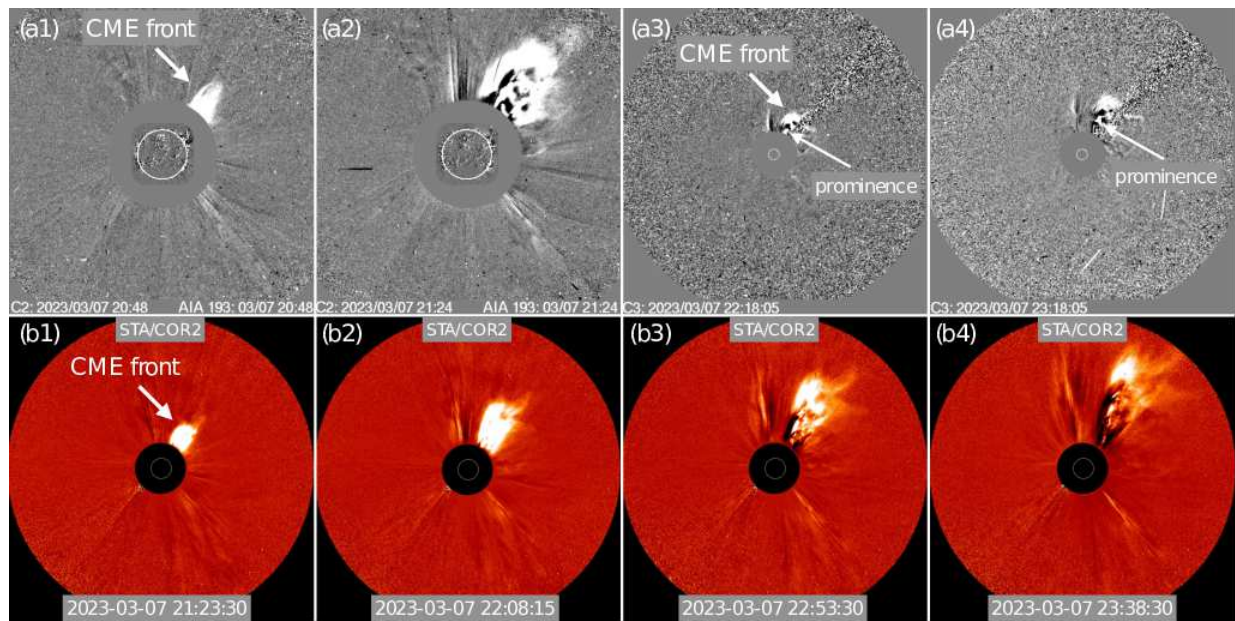


Figure 5. Running-difference images of the CME observed by LASCO-C2 and LASCO-C3 during 20:48–23:18 UT (top panels) and STA/COR2 during 21:23–23:38 UT (bottom panels). The white arrows point to the CME front and the following prominence. An animation showing the CME evolution is available. It covers a duration of 186 minutes from 20:48 UT to 23:54 UT on 2023 March 7. The entire movie runs for ~ 2 s. (An animation of this figure is available.)

The 3D reconstruction in this study aims to fit and track the leading edge of the prominence, while the two legs are incorporated in the cone as much as possible, which is different from the revised GCS model (Zhang et al. 2023a).

In Figure 7, the first column shows the prominence observed by AIA (a1) and EUVI (b1) at 20:25 UT. The second column shows the same images overlaid with projections of the reconstructed cone (cyan dots), where $\theta_1 = -40^\circ$, $r = 215'' \approx 155$ Mm, and $\omega = 34^\circ$. Likewise, the third and fourth columns show the prominence and cone ten minutes later, when $\theta_1 = -47^\circ$, $r = 395'' \approx 284$ Mm, and $\omega = 37^\circ$.

In Figure 8, the first and third columns show the prominence observed by AIA and EUV at 20:30 UT and 20:37 UT, respectively. The two legs of the prominence are distinguishable in the FOV of both instruments. However, owing to different viewing angles, the waist of the prominence looks slim in AIA images, but much wider in EUV images. The related cones are overlaid on the second and fourth columns. It is obvious that the cones track the leading edge of the prominence satisfactorily. The fitted parameters are listed in Table 2.

As mentioned before, observations of the fleet of instruments are out of phase. Consequently, it is difficult to trail the prominence from multiple viewpoints all the time. To get a complete trajectory of the prominence, we can still perform reconstructions by employing single-view observations from GONG, SUVI, EUV, and LASCO. As described at the beginning of Section 2, θ_2 and ϕ_2 are characteristics of the source region of an eruptive prominence or a CME. Assuming that the source region is fixed and invariable during the eruption, the values of θ_2 and ϕ_2 using multiview observations are applicable to single-view observations. Besides, using multiview observations, it is revealed that $\phi_1 = 0$, meaning that there is no longitudinal deflection. Hence, we use the same value of ϕ_1 in single-view observations. On the other hand, the values of r and ω are major characteristics of the cones and θ_1 denotes the latitudinal inclination angle of the cones. These three parameters change with time during the propagation. In Figure 9, the top panels show the prominence observed by SUVI during 20:28–20:43 UT. The bottom panels show the same EUV images superposed by projections of the cones (cyan dots). Similarly, the top and bottom panels of Figure 10 show the prominence observed by EUV during 21:00–21:45 UT and the corresponding cones, respectively. Thanks to the extraordinarily large FOV of EUV, the leading edge of the prominence is still visible nearly $3 R_\odot$ above the solar surface in EUV wavelengths. For the first time, Mierla et al. (2022) reported the detection of an eruptive prominence up to $>6 R_\odot$ in 304 \AA with EUV/FSI on board SOHO.

Figure 11 shows the CME observed by LASCO-C3 coronagraph during 22:18–23:54 UT and the reconstructed cones for the prominence (magenta dots). In panel (a), the green

arrow points to the bright CME front, which propagates in the northwest direction (see also Figure 5). The orange arrow points to the core of CME, which is the WL counterpart of the eruptive prominence following the bright front. Figures 9–11 demonstrate that reconstructions using single-view observations are plausible as well. Firstly, the tops of the reconstructed cones agree well with the leading edges of the prominence. Secondly, the two legs of the prominence are incorporated to the maximum extent. Combining observations of the prominence in $H\alpha$, EUV and WL passbands, a total of 38 moments during 20:15–23:54 UT (nearly four hours) are selected, when reconstructions are carried out. Figure 12 shows the Sun (yellow dots) and reconstructed cones for the prominence (magenta, green, and blue dots) as viewed from Earth (left column), side (middle column), and North Pole (right column) at three moments.

Temporal evolutions of the cone parameters are displayed in Figure 13. During the very early phase of prominence eruption between 20:15 UT and 20:45 UT, r increases monotonously from $118''$ to $640''$ (brown triangles in panel (b)), while ω increases from 30° to 37° and reaches a plateau (green diamonds in panel (a)). The corresponding values of l (Equation 3) also ramp up from $154''$ to $889''$ (orange boxes in panel (b)). Interestingly, the northward deflection of the prominence, which is characterized by $|\theta_1|$, first increases and then decreases (blue plus symbols in panel (a)). Using multiwavelength and multiview observations of the ‘‘Cartwheel CME’’ generated by a non-radial prominence eruption on 2008 April 9, Sahade et al. (2023) figured out the cause of double deflections of the prominence. The first deflection is due to the magnetic force directed toward a null point ($\mathbf{B} = 0$), and the second deflection is due to the magnetic pressure gradient of a coronal hole as the prominence rises up. The absolute value of non-radial tilt of the CME first increases and then decreases (see their Fig. 5). In our study, interaction between the prominence and large-scale, fan-shaped coronal loops in AR 13243 gives rise to a similar behavior of the prominence. Shen et al. (2011) investigated the influence of background magnetic field on the southward deflection of the CME at the early stage on 2007 October 8. It is concluded that the deflection may be caused by a nonuniform distribution of energy density of the background magnetic field ($U_{mag} = \frac{B^2}{8\pi}$). The CME is likely to move to the region with a lower magnetic-energy density. Using the GCS modeling (Thernisien et al. 2006), Gui et al. (2011) studied the deflections of 10 CMEs during their propagations and confirmed that the deflections are in good agreement with the gradient of magnetic-energy density (∇U_{mag}). Liu et al. (2024) performed 3D MHD simulations of non-radial solar eruptions. It is found that as the asymmetry of the distribution of magnetic flux at the photosphere increases, the eruption direction deviates further away from the radial path with

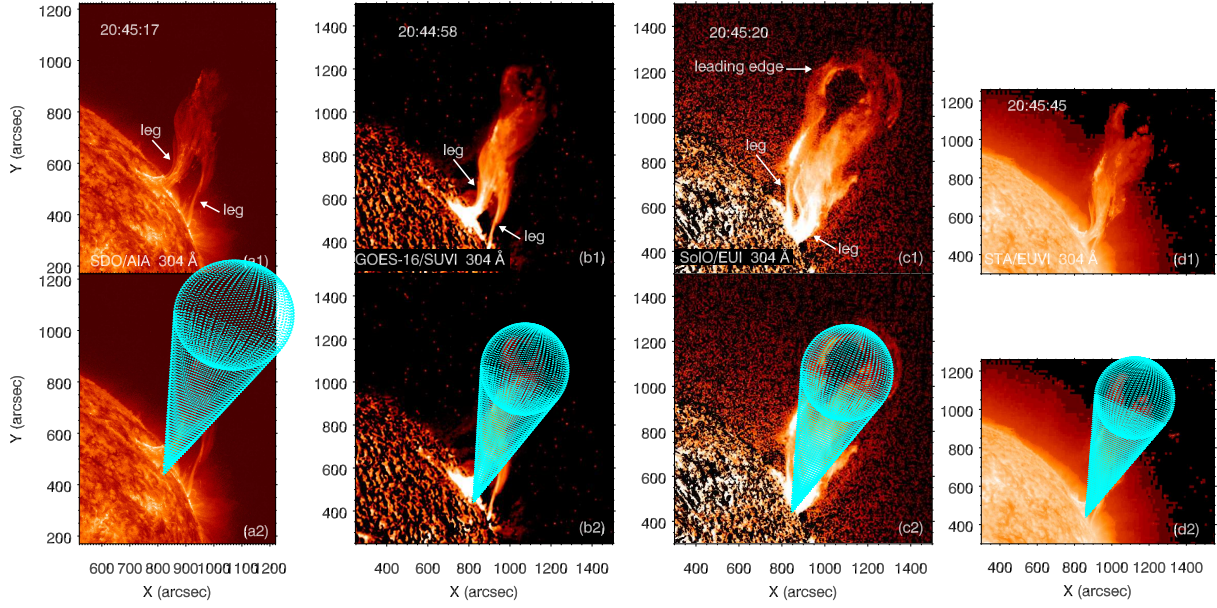


Figure 6. Top panels: the prominence observed in 304 \AA by SDO/AIA (a1), GOES-16/SUVI (b1), SoL/O/EUI (c1), and STA/EUVI (d1) around 20:45 UT. The white arrows point to the legs and leading edge of the prominence. Bottom panels: the same EUV images superposed by projections of the reconstructed cone (cyan dots).

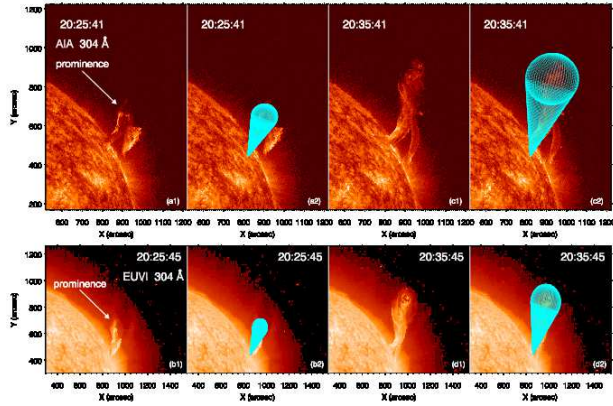


Figure 7. The prominence observed by AIA (top panels) and EUVI (bottom panels) at 20:25 UT (a1-b1) and 20:35 UT (c1-d1), respectively. Projections of the reconstructed cones are superposed with cyan dots (a2-d2).

a decreasing intensity. The eruption is strongly prohibited by an extraordinary asymmetry. In our study, the value of U_{mag} in the fan-like coronal loops is much larger than that to the northeast of prominence at the beginning of eruption. Consequently, the prominence deflects to the north and interacts with the loops, which are pushed aside during the rising motion (see Figure 3 and the online animation *Fig2.mp4*). After making a detour around the loops, the prominence continues to rise and outdistances the loops. There is no remarkable obstacle to cause northward deflection of the prominence anymore and the value of U_{mag} to the west of prominence is comparable to or slightly larger than that to the east. Hence, the

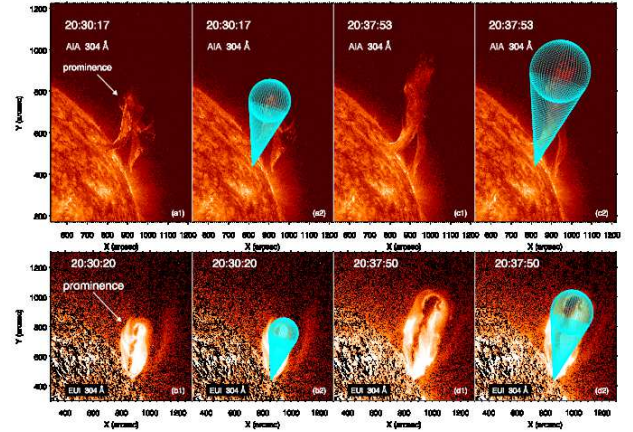


Figure 8. The prominence observed by AIA (top panels) and EUVI (bottom panels) at 20:30 UT (a1-b1) and 20:37 UT (c1-d1), respectively. Projections of the reconstructed cones are superposed with cyan dots (a2-d2).

absolute value of deflection angle (θ_1) decreases and plateaus at $\sim 36^\circ$.

In Figure 13, the northward deflection angle ($|\theta_1|$) of the prominence increases from $\sim 36^\circ$ to $\sim 47^\circ$ before returning to $\sim 36^\circ$ and keeping up. The angular width (ω) of the cone increases from $\sim 30^\circ$ to $\sim 37^\circ$ and remains unchanged after 20:29 UT (panel (a)). The leading edge height (l) of the prominence increases from $\sim 110 \text{ Mm}$ to $\sim 6400 \text{ Mm}$ (orange boxes in panel (b)). The heliocentric distance (h) of the prominence increases from ~ 1.1 to $10.0 R_\odot$ (green circles in panel (c)). It should be emphasized that we use multiwavelength observations to track the eruptive prominence. The

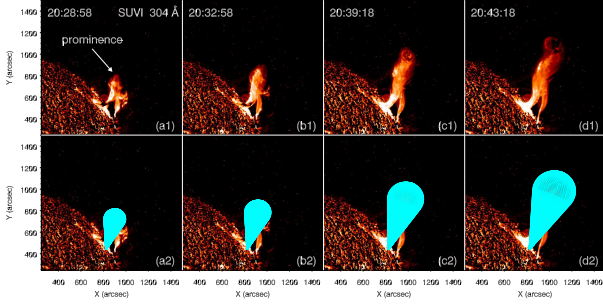


Figure 9. Top panels: the prominence observed by SUVI during 20:28–20:43 UT. Bottom panels: the same EUV images superposed by projections of the cones (cyan dots).

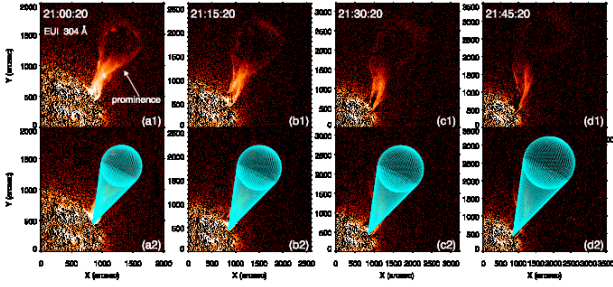


Figure 10. Top panels: the prominence observed by EUV during 21:00–21:45 UT. Bottom panels: the same EUV images superposed by projections of the cones (cyan dots).

eruptive prominence was observed in $H\alpha$ and EUV images during 20:15–21:45 UT, when h increased from 1.1 to 4.0 R_{\odot} . After leaving the FOVs of EUV images, the prominence was observed as the bright core of CME in LASCO-C3 WL images during 22:18–23:54 UT, when h increased from 5.6 to 10.0 R_{\odot} . A curve fitting using a quadratic function is applied to $h(t)$ during 20:15–22:30 UT, which is drawn with a green dashed line.

$$\frac{h(t)}{R_{\odot}} = 0.76 + 2.89 \times 10^{-1} \times t + 3.64 \times 10^{-8} \times t^2. \quad (6)$$

This function indicates continuing and coherent acceleration (50.7 m s^{-2}) of the eruptive prominence over two hours, which is comparable to the flare lifetime (Zhang et al. 2001). The acceleration is probably powered by flare magnetic reconnection underneath (Chen & Shibata 2000; Lin & Forbes 2000; Lynch et al. 2004). Such an evolution is evidently distinct from the two-step variation of active-region prominences or MFRs, which consists of a slow-rise phase and a fast-rise phase (Sterling & Moore 2005; Schrijver et al. 2008; Zhang et al. 2023b). The onset of fast rise is generally concurrent with the beginning of flare impulsive phase (Liewer et al. 2009; Yan et al. 2018; Cheng et al. 2020). In Figure 13(c), a linear fitting of $h(t)$ after 23:00 UT results in a true speed of $\sim 680 \text{ km s}^{-1}$ for the prominence. Height-time evolutions of the CME leading edge in the FOVs of

LASCO and STA/COR2 are drawn with purple and maroon circles, respectively. The apparent speeds of CME are ~ 788 and $\sim 598 \text{ km s}^{-1}$, respectively. The true speed of CME front is estimated to be $\sim 829 \text{ km s}^{-1}$, which is ~ 1.2 times larger than that of prominence.

4. DISCUSSION

As mentioned in Section 1, the triangulation method, normally using `scc_measure.pro` in SSW, is the main technique to recreate 3D structures of prominences. It has many advantages. Firstly, the whole body of a prominence, including the spine and two legs, could be reconstructed (Li et al. 2011; Zhou et al. 2017, 2021). Secondly, large-amplitude, vertical oscillation of a prominence (Zhang et al. 2024b) and rotation motion of a prominence during eruption have been unveiled (Bemporad 2009; Liewer et al. 2009; Joshi & Srivastava 2011; Thompson 2011; Thompson et al. 2012). Finally, non-radial propagation of a prominence could be followed (Joshi & Srivastava 2011; Bi et al. 2013). A combination of $H\alpha$, EUV, and WL observations allows us to track the prominence smoothly for ~ 4 hrs from the lower corona at the very beginning to a distance as far as $\sim 10 R_{\odot}$. Detour and continuous acceleration of the prominence are unambiguously demonstrated using the revised cone model.

There are limitations in our modeling. The cone is symmetrical, resembling an ice cream. Hence, it is solely employed to capture the leading edge of an eruptive prominence, rather than the two legs, which are incorporated as far as possible. Besides, rotation or rolling motions of a prominence are impossible to be reproduced up to now (Panaseuco et al. 2013). These difficulties might be overcome by the revised GCS model (Zhang et al. 2023a) or data-constrained MHD simulations (Guo et al. 2023). Moreover, it is a pity that multiview observations at some time are unavailable and we have to use single-view observations as complements, which is impossible to compare the results with multiview observations (Figures 9–11). The modeling would be undoubtedly preferred if multiview observations are available all the way. With the maximum of the 25th solar cycle approaching, the number of splendid and extreme eruptions is rapidly growing (Li et al. 2024). State-of-the-art telescopes are ready to capture these activities, such as the Chinese $H\alpha$ Solar Explorer (CHASE; Li et al. 2022) and the Advanced Space-Based Solar Observatory (ASO-S; Gan et al. 2023). Additional case studies are worthwhile to trace the evolutions of prominences more precisely and more thoroughly. Applications of the forward modeling techniques to 3D reconstructions of prominences and CMEs are very important and desirable to the space weather forecast.

5. CONCLUSION

In this paper, we carry out multiwavelength and multiview observations of the prominence eruption, which generates a

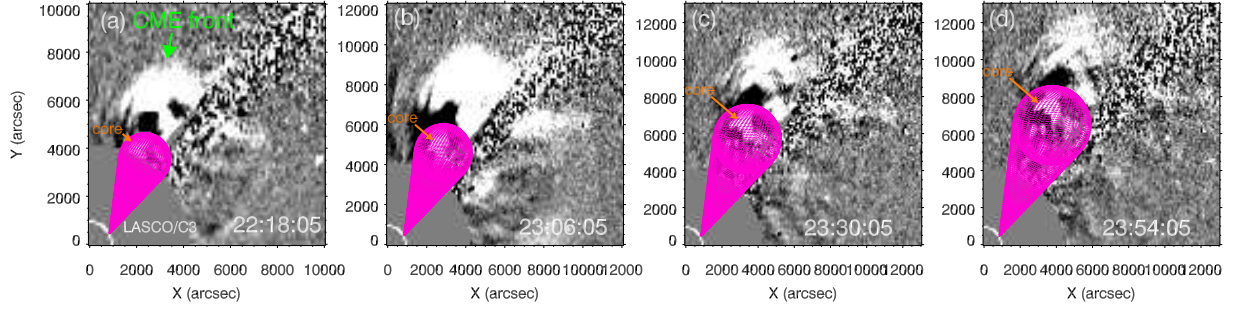


Figure 11. The CME observed by LASCO-C3 coronagraph during 22:18–23:54 UT and the reconstructed cones for the prominence (magenta dots). The orange arrows point to the CME core. In panel (a), the green arrow points to the bright front of CME.

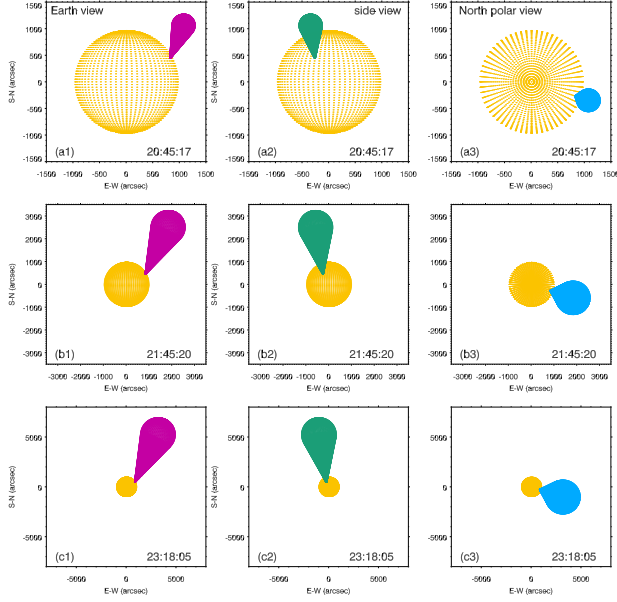


Figure 12. The Sun (yellow dots) and reconstructed cones for the prominence (magenta, green, and blue dots) as viewed from Earth (left column), side (middle column), and North Pole (right column) at 20:45 UT (top row), 21:45 UT (middle row), and 23:18 UT (bottom row).

C2.3 class flare and a CME on 2023 March 7. Using the revised cone model, the leading edge of the prominence is well tracked. The direction and kinetic evolution of the prominence are obtained for nearly four hours. The main results are as follows:

1. The prominence propagates non-radially and makes a detour around the large-scale coronal loops in AR 13243. The northward deflection angle increases from $\sim 36^\circ$ to $\sim 47^\circ$ before returning to $\sim 36^\circ$ and keeping up. There is no longitudinal deflection throughout the propagation.
2. The angular width of the cone increases from $\sim 30^\circ$ and reaches a plateau at $\sim 37^\circ$. The heliocentric distance of the prominence rises from ~ 1.1 to $\sim 10.0 R_\odot$, and the prominence experiences continuous accelera-

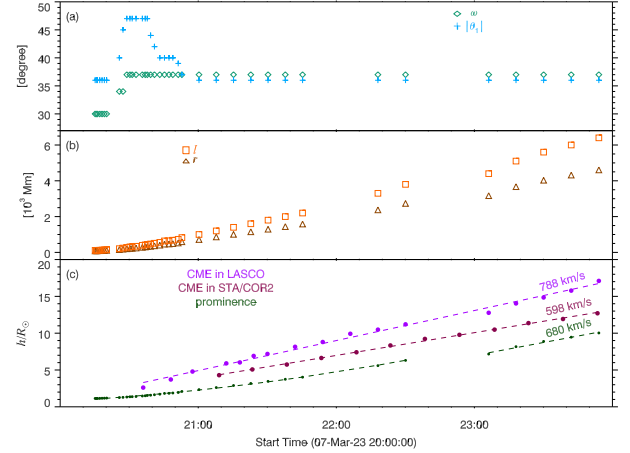


Figure 13. (a)–(b) Temporal evolutions of the deflection angle (blue “+” symbol), angular width (green diamonds), r (brown triangles), and total length (orange boxes) of the reconstructed cones, respectively. (c) Temporal evolution of the heliocentric distance of the cones (green circles) and height variations of the bright front of the fan-like CME in the FOVs of LASCO (purple circles) and STA/COR2 (maroon circles). Linear speeds (~ 788 and ~ 598 km s^{-1}) of the CME throughout the propagation and linear speed (~ 680 km s^{-1}) of the prominence after 23:00 UT are labeled. A quadratic polynomial is used to perform curve fitting of $h(t)$ during 20:15–22:30 UT.

tion (~ 51 m s^{-2}) over two hours, which is probably related to the magnetic reconnection during the flare. The true speed of CME front is estimated to be ~ 829 km s^{-1} , which is ~ 1.2 times larger than that of CME core (prominence). This is the first attempt of applying the revised cone model to 3D reconstruction and tracking of eruptive prominences, including the acceleration and deflection.

The authors appreciate the reviewer for valuable comments and suggestions to improve the quality of this article. This work utilizes GONG data obtained by the NSO Integrated Synoptic Program, managed by the National Solar Observatory, which is operated by the Association of Universities for Research in Astronomy (AURA), Inc. under a cooperative agreement with the National Science Foundation and with contribution from the National Oceanic and Atmospheric Administration. The GONG network of instruments is hosted by the Big Bear Solar Observatory, High Altitude Observatory, Learmonth Solar Observatory, Udaipur Solar Observatory, Instituto de Astrofísica de Canarias, and Cerro Tololo Interamerican Observatory. SDO is a mission of NASA's Living With a Star Program. AIA data are courtesy of the NASA/SDO science teams. Solar Orbiter is a space mission of international collaboration between ESA and NASA, operated by ESA. The Extreme Ultraviolet Imager (EUI) is part of the remote sensing instrument package of the ESA/NASA Solar Orbiter mission. The EUI consists of three telescopes, the Full Sun Imager (FSI) and two High Resolution Imagers (HRILYA, HRIEUV), which are optimised to image in Lyman- α and EUV (17.4 nm, 30.4 nm). The 3 telescopes together provide a coverage from chromosphere up to corona with both high resolution and with a wide field of view. EUI scientific data consists of calibrated and raw data images acquired by the three EUI telescopes. Following the orbit profile of Solar Orbiter, the data coverage, imaging cadence and effective spatial resolution of the EUI data are very variable. "SolO/EUI data release 6.0" was initially released with the Solar Orbiter/EUI data up till mid 2023 January. Later data will be included a-posteriori in this release as long as the software (including calibration) remains stable that generates the science data products. SUVI was designed and built at Lockheed-Martin's Advanced Technology Center in Palo Alto, California. STEREO/SECCHI data are provided by a consortium of US, UK, Germany, Belgium, and France. This work is supported by the Strategic Priority Research Program of the Chinese Academy of Sciences, Grant No. XDB0560000, the National Key R&D Program of China 2021YFA1600500 (2021YFA1600502), 2022YFF0503003 (2022YFF0503000), NSFC under the grant numbers 12373065, 42174201, and 12173049, Natural Science Foundation of Jiangsu Province (BK20231510), Project Supported by the Specialized Research Fund for State Key Laboratories, and Yunnan Key Laboratory of Solar Physics and Space Science under the grant number YN-SPCC202206.

REFERENCES

Awasthi, A. K., Liu, R., & Wang, Y. 2019, *ApJ*, 872, 109.
doi:10.3847/1538-4357/aafdad

Bemporad, A. 2009, *ApJ*, 701, 298.
doi:10.1088/0004-637X/701/1/298

- Berger, T. E., Slater, G., Hurlburt, N., et al. 2010, *ApJ*, 716, 1288. doi:10.1088/0004-637X/716/2/1288
- Bi, Y., Jiang, Y., Yang, J., et al. 2013, *ApJ*, 773, 162. doi:10.1088/0004-637X/773/2/162
- Brueckner, G. E., Howard, R. A., Koomen, M. J., et al. 1995, *SoPh*, 162, 357. doi:10.1007/BF00733434
- Chen, P. F. 2011, *Living Reviews in Solar Physics*, 8, 1. doi:10.12942/lrsp-2011-1
- Chen, P. F. & Shibata, K. 2000, *ApJ*, 545, 524. doi:10.1086/317803
- Cheng, X., Zhang, J., Kliem, B., et al. 2020, *ApJ*, 894, 85. doi:10.3847/1538-4357/ab886a
- Dai, J., Zhang, Q., Qiu, Y., et al. 2023, *ApJ*, 959, 71. doi:10.3847/1538-4357/ad0839
- Fan, Y. 2005, *ApJ*, 630, 543. doi:10.1086/431733
- Feng, L., Inhester, B., Wei, Y., et al. 2012, *ApJ*, 751, 18. doi:10.1088/0004-637X/751/1/18
- Fletcher, L. 2024, *ARA&A*, 62, 437. doi:10.1146/annurev-astro-052920-010547
- Gan, W., Zhu, C., Deng, Y., et al. 2023, *SoPh*, 298, 68. doi:10.1007/s11207-023-02166-x
- Georgoulis, M. K., Nindos, A., & Zhang, H. 2019, *Philosophical Transactions of the Royal Society of London Series A*, 377, 20180094. doi:10.1098/rsta.2018.0094
- Gieseler, J., Dresing, N., Palmroos, C., et al. 2023, *Frontiers in Astronomy and Space Sciences*, 9, 384. doi:10.3389/fspas.2022.1058810
- Guo, Y., Schmieder, B., Démoulin, P., et al. 2010, *ApJ*, 714, 343. doi:10.1088/0004-637X/714/1/343
- Guo, Y., Xu, Y., Ding, M. D., et al. 2019, *ApJL*, 884, L1. doi:10.3847/2041-8213/ab4514
- Guo, J. H., Qiu, Y., Ni, Y. W., et al. 2023, *ApJ*, 956, 119. doi:10.3847/1538-4357/acf198
- Gui, B., Shen, C., Wang, Y., et al. 2011, *SoPh*, 271, 111. doi:10.1007/s11207-011-9791-9
- Hou, Y., Li, C., Li, T., et al. 2023, *ApJ*, 959, 69. doi:10.3847/1538-4357/ad08bd
- Howard, T. A., Webb, D. F., Tappin, S. J., et al. 2006, *Journal of Geophysical Research (Space Physics)*, 111, A04105. doi:10.1029/2005JA011349
- Howard, R. A., Moses, J. D., Vourlidas, A., et al. 2008, *SSRv*, 136, 67. doi:10.1007/s11214-008-9341-4
- Howard, T. A. 2015, *ApJ*, 806, 176. doi:10.1088/0004-637X/806/2/176
- Illing, R. M. E. & Hundhausen, A. J. 1985, *J. Geophys. Res.*, 90, 275. doi:10.1029/JA090iA01p00275
- Isavnin, A. 2016, *ApJ*, 833, 267. doi:10.3847/1538-4357/833/2/267
- Ji, H., Wang, H., Schmahl, E. J., et al. 2003, *ApJL*, 595, L135. doi:10.1086/378178
- Joshi, A. D. & Srivastava, N. 2011, *ApJ*, 730, 104. doi:10.1088/0004-637X/730/2/104
- Kaiser, M. L., Kucera, T. A., Davila, J. M., et al. 2008, *SSRv*, 136, 5. doi:10.1007/s11214-007-9277-0
- Karpen, J. T., Tanner, S. E. M., Antiochos, S. K., et al. 2005, *ApJ*, 635, 1319. doi:10.1086/497531
- Kilpua, E. K. J., Lugaz, N., Mays, M. L., et al. 2019, *Space Weather*, 17, 498. doi:10.1029/2018SW001944
- Labrosse, N., Heinzel, P., Vial, J.-C., et al. 2010, *SSRv*, 151, 243. doi:10.1007/s11214-010-9630-6
- Lemen, J. R., Title, A. M., Akin, D. J., et al. 2012, *SoPh*, 275, 17. doi:10.1007/s11207-011-9776-8
- Li, T., Zhang, J., Zhang, Y., et al. 2011, *ApJ*, 739, 43. doi:10.1088/0004-637X/739/1/43
- Li, C., Fang, C., Li, Z., et al. 2022, *Science China Physics, Mechanics, and Astronomy*, 65, 289602. doi:10.1007/s11433-022-1893-3
- Li, Y., Liu, X., Jing, Z., et al. 2024, *ApJL*, 972, L1. doi:10.3847/2041-8213/ad6d6c
- Liewer, P. C., De Jong, E. M., Hall, J. R., et al. 2009, *SoPh*, 256, 57. doi:10.1007/s11207-009-9363-4
- Lin, J. & Forbes, T. G. 2000, *J. Geophys. Res.*, 105, 2375. doi:10.1029/1999JA900477
- Lin, Y., Engvold, O., der Voort, L. R. van., et al. 2005, *SoPh*, 226, 239. doi:10.1007/s11207-005-6876-3
- Liu, R., Alexander, D., & Gilbert, H. R. 2007, *ApJ*, 661, 1260. doi:10.1086/513269
- Liu, R., Kliem, B., Török, T., et al. 2012, *ApJ*, 756, 59. doi:10.1088/0004-637X/756/1/59
- Liu, Q., Jiang, C., Feng, X., et al. 2024, *MNRAS*, 533, L25. doi:10.1093/mnras/slae057
- Lynch, B. J., Antiochos, S. K., MacNeice, P. J., et al. 2004, *ApJ*, 617, 589. doi:10.1086/424564
- Mackay, D. H., Karpen, J. T., Ballester, J. L., et al. 2010, *SSRv*, 151, 333. doi:10.1007/s11214-010-9628-0
- Michalek, G., Gopalswamy, N., & Yashiro, S. 2003, *ApJ*, 584, 472. doi:10.1086/345526
- Mierla, M., Davila, J., Thompson, W., et al. 2008, *SoPh*, 252, 385. doi:10.1007/s11207-008-9267-8
- Mierla, M., Inhester, B., Antunes, A., et al. 2010, *Annales Geophysicae*, 28, 203. doi:10.5194/angeo-28-203-2010
- Mierla, M., Zhukov, A. N., Berghmans, D., et al. 2022, *A&A*, 662, L5. doi:10.1051/0004-6361/202244020
- Moran, T. G. & Davila, J. M. 2004, *Science*, 305, 66. doi:10.1126/science.1098937
- Müller, D., St. Cyr, O. C., Zouganelis, I., et al. 2020, *A&A*, 642, A1. doi:10.1051/0004-6361/202038467
- Okamoto, T. J., Tsuneta, S., Berger, T. E., et al. 2007, *Science*, 318, 1577. doi:10.1126/science.1145447
- Panasenco, O., Martin, S., Joshi, A. D., et al. 2011, *Journal of Atmospheric and Solar-Terrestrial Physics*, 73, 1129. doi:10.1016/j.jastp.2010.09.010

- Panasenco, O., Martin, S. F., Velli, M., et al. 2013, *SoPh*, 287, 391.
doi:10.1007/s11207-012-0194-3
- Parenti, S. 2014, *Living Reviews in Solar Physics*, 11, 1.
doi:10.12942/lrsp-2014-1
- Pesnell, W. D., Thompson, B. J., & Chamberlin, P. C. 2012, *SoPh*, 275, 3. doi:10.1007/s11207-011-9841-3
- Rochus, P., Auchère, F., Berghmans, D., et al. 2020, *A&A*, 642, A8. doi:10.1051/0004-6361/201936663
- Ruan, G., Chen, Y., Wang, S., et al. 2014, *ApJ*, 784, 165.
doi:10.1088/0004-637X/784/2/165
- Rust, D. M. & Kumar, A. 1996, *ApJL*, 464, L199.
doi:10.1086/310118
- Sahade, A., Vourlidas, A., Balmaceda, L. A., et al. 2023, *ApJ*, 953, 150. doi:10.3847/1538-4357/ace420
- Schrijver, C. J., Elmore, C., Kliem, B., et al. 2008, *ApJ*, 674, 586.
doi:10.1086/524294
- Schwenn, R., dal Lago, A., Huttunen, E., et al. 2005, *Annales Geophysicae*, 23, 1033. doi:10.5194/angeo-23-1033-2005
- Seaton, D. B. & Darnel, J. M. 2018, *ApJL*, 852, L9.
doi:10.3847/2041-8213/aaa28e
- Shen, C., Wang, Y., Gui, B., et al. 2011, *SoPh*, 269, 389.
doi:10.1007/s11207-011-9715-8
- Shen, Y., Liu, Y., & Su, J. 2012, *ApJ*, 750, 12.
doi:10.1088/0004-637X/750/1/12
- Song, H., Zhang, J., Li, L., et al. 2023a, *ApJ*, 942, 19.
doi:10.3847/1538-4357/aca6e0
- Sterling, A. C. & Moore, R. L. 2005, *ApJ*, 630, 1148.
doi:10.1086/432044
- Tadikonda, S. K., Freesland, D. C., Minor, R. R., et al. 2019, *SoPh*, 294, 28. doi:10.1007/s11207-019-1411-0
- Teng, W., Su, Y., Liu, R., et al. 2024, *ApJ*, 970, 100.
doi:10.3847/1538-4357/ad50d0
- Thernisien, A. F. R., Howard, R. A., & Vourlidas, A. 2006, *ApJ*, 652, 763. doi:10.1086/508254
- Thompson, W. T. 2011, *Journal of Atmospheric and Solar-Terrestrial Physics*, 73, 1138.
doi:10.1016/j.jastp.2010.07.005
- Thompson, W. T., Kliem, B., & Török, T. 2012, *SoPh*, 276, 241.
doi:10.1007/s11207-011-9868-5
- Török, T., Kliem, B., & Titov, V. S. 2004, *A&A*, 413, L27.
doi:10.1051/0004-6361:20031691
- Valori, G., Kliem, B., & Keppens, R. 2005, *A&A*, 433, 335.
doi:10.1051/0004-6361:20042008
- van Ballegoijen, A. A. 2004, *ApJ*, 612, 519. doi:10.1086/422512
- Vial, J.-C. & Engvold, O. 2015, *Solar Prominences*, 415.
doi:10.1007/978-3-319-10416-4
- Wang, J., Li, D., Li, C., et al. 2024, *ApJL*, 965, L28.
doi:10.3847/2041-8213/ad3af8
- Weiss, A. J., Möstl, C., Amerstorfer, T., et al. 2021, *ApJS*, 252, 9.
doi:10.3847/1538-4365/abc9bd
- Wei, H., Huang, Z., Li, C., et al. 2023, *ApJ*, 958, 116.
doi:10.3847/1538-4357/acf569
- Wiegelmann, T., Inhester, B., & Sakurai, T. 2006, *SoPh*, 233, 215.
doi:10.1007/s11207-006-2092-z
- Xia, C. & Keppens, R. 2016, *ApJ*, 823, 22.
doi:10.3847/0004-637X/823/1/22
- Xie, H., Ofman, L., & Lawrence, G. 2004, *Journal of Geophysical Research (Space Physics)*, 109, A03109.
doi:10.1029/2003JA010226
- Yan, X. L., Xue, Z. K., Pan, G. M., et al. 2015, *ApJS*, 219, 17.
doi:10.1088/0067-0049/219/2/17
- Yan, X. L., Yang, L. H., Xue, Z. K., et al. 2018, *ApJL*, 853, L18.
doi:10.3847/2041-8213/aaa6c2
- Yang, L., Yan, X., Li, T., et al. 2017, *ApJ*, 838, 131.
doi:10.3847/1538-4357/aa653a
- Zhang, J., Dere, K. P., Howard, R. A., et al. 2001, *ApJ*, 559, 452.
doi:10.1086/322405
- Zhang, Q. M. 2021, *A&A*, 653, L2.
doi:10.1051/0004-6361/202141982
- Zhang, Q. M. 2022, *A&A*, 660, A144.
doi:10.1051/0004-6361/202142942
- Zhang, Q. M., Chen, J. L., Li, S. T., et al. 2022, *SoPh*, 297, 18.
doi:10.1007/s11207-022-01952-3
- Zhang, Q.-M., Hou, Z.-Y., & Bai, X.-Y. 2023a, *Research in Astronomy and Astrophysics*, 23, 125004.
doi:10.1088/1674-4527/acee4d
- Zhang, Q., Teng, W., Li, D., et al. 2023b, *ApJ*, 958, 85.
doi:10.3847/1538-4357/ad05bc
- Zhang, Q. M., Lin, M. S., Yan, X. L., et al. 2024, *MNRAS*, 533, 3255. doi:10.1093/mnras/stae1936
- Zhang, Y., Zhang, Q., Song, D., et al. 2024, *ApJ*, 963, 140.
doi:10.3847/1538-4357/ad206d
- Zhao, X. P., Plunkett, S. P., & Liu, W. 2002, *Journal of Geophysical Research (Space Physics)*, 107, 1223.
doi:10.1029/2001JA009143
- Zhong, Z., Guo, Y., & Ding, M. D. 2021, *Nature Communications*, 12, 2734. doi:10.1038/s41467-021-23037-8
- Zhou, Z., Zhang, J., Wang, Y., et al. 2017, *ApJ*, 851, 133.
doi:10.3847/1538-4357/aa9bd9
- Zhou, C., Xia, C., & Shen, Y. 2021, *A&A*, 647, A112.
doi:10.1051/0004-6361/202039558
- Zhou, Y., Ji, H., & Zhang, Q. 2023, *SoPh*, 298, 35.
doi:10.1007/s11207-023-02126-5
- Zirker, J. B., Engvold, O., & Martin, S. F. 1998, *Nature*, 396, 440.
doi:10.1038/24798